GRADIENT CALCULATION FOR WAVEFORM INVERSION OF MICROSEISMIC DATA IN VTI MEDIA

OSCAR JARILLO MICHEL and ILYA TSVANKIN

Center for Wave Phenomena, Colorado School of Mines, Golden, CO 80401, U.S.A.
ojarillo@mymail.mines.edu, ilya@dix.mines.edu

ABSTRACT

Jarillo Michel, O. and Tsvankin, I., 2014. Gradient calculation for waveform inversion of microseismic data in VTI media. *Journal of Seismic Exploration*, 23: 201-217.

In microseismic data processing, source locations and origin times are usually obtained using kinematic techniques, whereas moment-tensor estimates are typically based on linear inversion of P- and S-wave amplitudes. Waveform inversion (WI) can potentially provide more accurate source parameters along with an improved velocity model by incorporating information contained in the entire trace including the coda. Here, we address one of the key issues in implementing WI for microseismic surveys - efficient calculation of the gradient of the objective function with respect to the model parameters. Application of the adjoint-state method helps obtain closed-form expressions for the gradient with respect to the source location, origin time, and moment tensor. Computation of the forward and adjoint wavefields is performed with a finite-difference algorithm that handles elastic VTI (transversely isotropic with a vertical symmetry axis) models. Numerical examples illustrate the properties of the gradient for multicomponent data recorded by a vertical receiver array placed in homogeneous and horizontally layered VTI media.

KEY WORDS: microseismic, waveform inversion, anisotropy, transverse isotropy, adjoint-state method, multicomponent data, source location, moment tensor.

INTRODUCTION

Microseismicity has developed in recent years as an efficient technique for monitoring of hydraulic fractures and the surrounding reservoir volume (Maxwell, 2010; Kendall et al., 2011). Microseismic experiments typically involve recording the seismic response to hydraulic fracturing of tight reservoirs, most often shales. The location of the induced microfractures, as well as the origin time of the corresponding seismic events can be inferred from the data acquired in an observation borehole or at the surface. Usually only a single borehole is available, but it is highly beneficial to record microseismic data in several boreholes.

Accurate location of microseismic events requires knowledge of the background velocity model. This initial model is usually obtained from sonic logs and traveltimes of the direct P- and S-waves excited by perforation shots and recorded by geophones deployed in a monitor borehole. Afterwards, the model can be updated using the traveltimes or waveforms of microseismic events. Velocity analysis without adequately accounting for seismic anisotropy may lead to significant errors in event location (Van Dok et al., 2011). In particular, shales are known to be transversely isotropic and may become orthorhombic or possess an even lower symmetry due to fracturing (Tsvankin and Grechka, 2011; Tsvankin, 2012).

Depending on the receiver geometry and spatial distribution of sources, microseismic data can help estimate the pertinent anisotropy parameters (Grechka and Duchkov, 2011) simultaneously with event location. For example, Grechka et al. (2011) prove that anisotropic velocity models constructed from traveltimes while locating microseismic events provide more accurate source locations than those obtained without accounting for anisotropy. Also, Li et al. (2013) show that building VTI velocity models simultaneously with event location significantly reduces the traveltime residuals compared to standard location techniques that employ isotropic velocity models obtained from sonic logs and perforation shots. Grechka and Yaskevich (2013, 2014) demonstrate that for microseismic surveys with sufficient angle coverage it is possible to construct layered triclinic models and substantially improve the accuracy of event location.

Still, kinematic inversion essentially replaces a seismic trace with the δ-functions corresponding to the traveltimes of the direct arrivals, which restricts the resolution of event location according to the Rayleigh criterion (i.e., two sources are indistinguishable if the distance between them is smaller than one-half of the predominant wavelength). Considering the rapidly increasing usage of back-projection techniques and the rich information content of microseismic data, improved results can be expected from waveform inversion (WI). Indeed, WI operates with the entire trace including scattered waves, so location results are not subject to the Rayleigh criterion. Hence, for wavelengths typical in downhole microseismic surveys, one can expect substantially reduced event-location errors. Another potential benefit of WI, not explored in this paper, is an improved accuracy of the velocity model.

The source mechanism of microseismic events can reveal important information about the rupture process. Point earthquake sources are described by the second-rank symmetric seismic moment tensor $\mathbf{M}$. As discussed by Vavryčuk (2007), all six independent elements of $\mathbf{M}$ for microseismic events can be retrieved from the amplitudes of P-waves recorded in three boreholes or from P-, SV-, and SH-wave amplitudes measured in two boreholes. For sources and receivers located in the $[x_1, x_3]$-plane of a VTI model, the in-plane polarized

waves depend on the elements M_{11}, M_{13}, and M_{33}, which potentially can be found by inverting P- and SV-waveforms recorded in a single borehole. In practice, $\mathbf{M}$ is obtained independently of other microseismic parameters by linear inversion of P- and S-wave amplitudes. Since WI incorporates waveform information, it may provide improved estimates of $\mathbf{M}$ and, at the same time, carry out event location and constrain the origin time.

Waveform inversion is used to build high-resolution velocity models from seismic data using phase and, sometimes, amplitude information (Tarantola, 1984; Gauthier et al., 1986; Mora, 1987; Pratt, 1999; Virieux and Operto, 2009). Recently WI has been extended to elastic and anisotropic media (Lee et al., 2010; Kamath and Tsvankin, 2013), which makes it suitable for multicomponent reflection and microseismic data.

The objective function in WI quantifies the difference between observed and predicted data in the time or frequency domain. Efficient inversion requires application of iterative optimization schemes such as gradient-based methods, which involve calculation of the gradient of the objective function with respect to the model parameters. In principle, the gradient can be found from the Fréchet derivatives obtained by differentiating the wavefield with respect to each model parameter. However, if the number of unknowns is large, computation of the Fréchet derivatives becomes prohibitively expensive.

A computationally efficient alternative for computing the gradient without the Fréchet derivatives is the adjoint-state method (Plessix, 2006; Fichtner, 2006, 2009; Köhn, 2011). This method makes it possible to calculate the gradient using just two forward-modeling simulations: first to generate the forward wavefield (predicted data), and second to compute the adjoint wavefield.

There has been significant progress in applying adjoint methods to tomographic velocity analysis and source-parameter inversion in global seismology. Tromp et al. (2005) and Liu and Tromp (2006) employ an adjoint formulation based on the Lagrangian-multiplier method to derive the gradient for estimating the P- and S-wave velocities in isotropic media. They also analyze the sensitivity (Fréchet) kernels for 2D and 3D velocity models. Kim et al. (2011) obtain gradient expressions for the source parameters using the adjoint-state method. They also implement conjugate-gradient inversion to estimate the source location and moment tensor for two earthquakes in Southern California using a known isotropic velocity model. Morency and Mellors (2012) follow the same approach to evaluate the source parameters of a geothermal event.

Here, we discuss gradient calculation for waveform inversion of microseismic data in heterogeneous VTI media. The current algorithm is

designed to estimate the source location, origin time, and moment tensor from 2D microseismic experiments.

We start by describing 2D elastic finite-difference modeling for dislocation-type sources embedded in a VTI medium. Then we discuss application of the adjoint-state method to compute the gradient for waveform inversion. Efficient gradient calculation is implemented by adapting to our problem the general expressions for the gradient obtained by Kim et al. (2011). Although the interval Thomsen parameters of layered VTI media can be estimated by WI as well, the current formulation is limited to the gradient for the source parameters. The performance of the algorithm is illustrated by synthetic tests for homogeneous and layered VTI media. The examples display multicomponent wavefields obtained by forward and adjoint finite-difference modeling and help understand the properties of the objective-function derivatives for the source location, origin time, and moment tensor.

GRADIENT FROM THE ADJOINT-STATE METHOD

Forward problem

The wave equation for a heterogeneous anisotropic medium can be written as:

$$\rho(\partial^2 u_i/\partial t^2) - \partial[c_{ijkl}(\partial u_k/\partial x_l)]/\partial x_j = f_i \ , \tag{1}$$

where $\mathbf{u}(\mathbf{x},t)$ is the displacement field, t is time, c_{ijkl} is the stiffness tensor ($i,j,k,l = 1,2,3$), $\rho(x)$ is density, and $\mathbf{f}(x,t)$ is the body force density.

Dislocation-type sources are described by the seismic moment tensor,

$$\mathbf{M} = \begin{pmatrix} M_{11} & M_{12} & M_{13} \\ M_{21} & M_{22} & M_{23} \\ M_{31} & M_{32} & M_{33} \end{pmatrix} \ , \tag{2}$$

which can be incorporated into the source term of eq. (1) by using the notion of equivalent force (Aki and Richards, 1980; Dahlen and Tromp, 1998):

$$\rho(\partial^2 u_i/\partial t^2) - \partial[c_{ijkl}(\partial u_k/\partial x_l)]/\partial x_j = -M_{ij}\{\partial[\delta(\mathbf{x} - \mathbf{x}^S)/\partial x_j\}S(t) \ , \tag{3}$$

where $\mathbf{x}^S$ is the source location, $S(t)$ is the source time function, and $\delta(\mathbf{x} - \mathbf{x}^S)$ is the spatial δ-function. We use a finite-difference (FD) algorithm to obtain exact solutions of eq. (3).

Modeling examples

Forward modeling for gradient calculation in VTI media is carried out with the elastic finite-difference program sfewe in MADAGASCAR. The model is described by the interval Thomsen parameters - the P- and S-wave vertical velocities V_{P0} and V_{S0} and the anisotropy coefficients ε and δ defined as (Thomsen, 1986; Tsvankin, 2012):

$$\varepsilon \equiv (c_{11} - c_{33})/(2c_{33}) \ , \tag{4}$$

$$\delta \equiv [(c_{13} + c_{55})^2 - (c_{33} - c_{55})^2]/[2c_{33}(c_{33} - c_{55})] \ . \tag{5}$$

Note that P- and SV-waves propagating in the $[x_1,x_3]$-plane are not influenced by the Thomsen parameter γ. An important combination of Thomsen parameters is the coefficient $\sigma \equiv (V_{P0}/V_{S0})^2(\varepsilon - \delta)$, which is largely responsible for the kinematic signatures of SV-waves.

The relevant elements of **M** for the in-plane polarized waves (P and SV) from a dislocation source in a VTI medium can be represented as (Aki and Richards, 1980; Vavryčuk, 2005):

$$M_{11} = \Sigma \, \bar{u} \, \nu_3 \, s_3 \, (c_{13} - c_{11}) \ , \tag{6}$$

$$M_{13} = \Sigma \, \bar{u} \, (\nu_1 \, s_3 + \nu_3 \, s_1) \, c_{55} \ , \tag{7}$$

$$M_{33} = \Sigma \, \bar{u} \, \nu_3 \, s_3 \, (c_{33} - c_{13}) \ , \tag{8}$$

where Σ is the fault area, $\bar{u}$ is the magnitude of slip (displacement discontinuity), ν is the unit fault normal, **s** is the unit vector in the slip direction, and c_{11}, c_{13}, c_{33}, and c_{55} are the stiffness coefficients in the two-index Voigt notation (Fig. 1). Because the vectors ν and **s** are confined to the $[x_1,x_3]$-plane, eqs. (6) - (8) for dip-slip sources can be expressed as a function of the fault dip angle θ. Taking into account that $\nu_1 = \sin\theta$, $\nu_3 = \cos\theta$, $s_1 = \cos\theta$, and $s_3 = -\sin\theta$, we rewrite eqs. (6) - (8) as:

$$M_{11} = (-\Sigma \, \bar{u}/2) \sin2\theta \, (c_{13} - c_{11}) \ , \tag{9}$$

$$M_{13} = \Sigma \, \bar{u} \cos2\theta \, c_{55} \ , \tag{10}$$

$$M_{33} = (-\Sigma \, \bar{u}/2) \sin2\theta \, (c_{33} - c_{13}) \ . \tag{11}$$

The wavefields generated by dislocation-type sources in a homogeneous VTI medium are shown in Fig. 2. The amplitude distribution and intensity of the P- and S-waves change substantially with the fault orientation. Because the magnitude of σ is relatively large (close to unity), the SV-wavefront exhibits triplications at oblique propagation directions (Tsvankin, 2012).
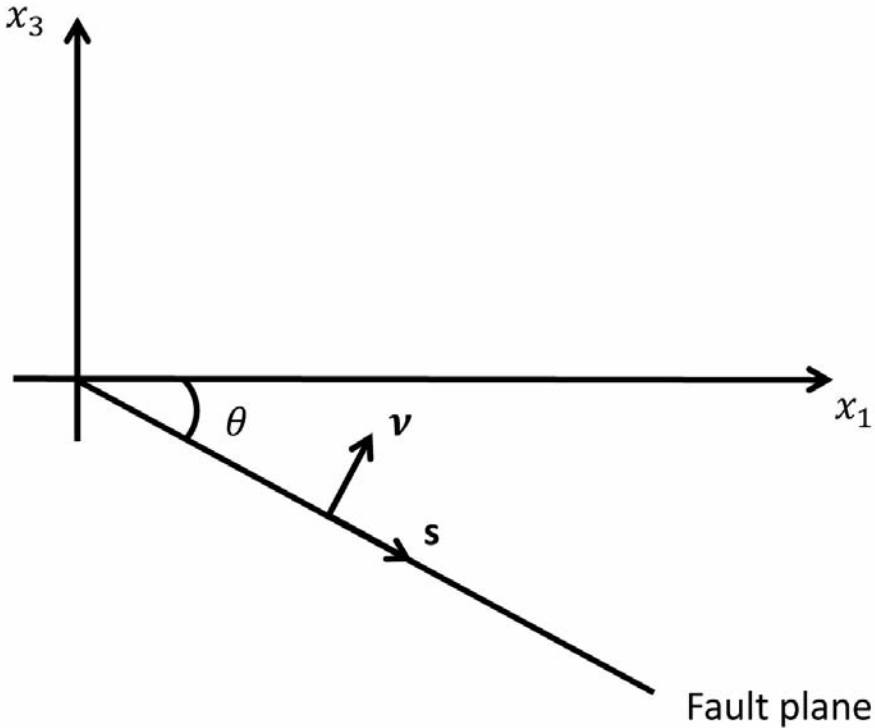
Fig. 1. 2D fault geometry used in forward modeling. The dip angle θ ($0° \leq \theta \leq 90°$) is measured down from the horizontal axis. The incidence plane $[x_1, x_3]$ is assumed to coincide with the dip plane of the fault and contain the slip **s**.

Inverse problem

As mentioned above, the P- and SV-waves recorded in the $[x_1, x_3]$-plane depend on the components M_{11}, M_{13}, and M_{33} of the moment tensor. Here, our goal is to invert just for the three moment-tensor elements, the source coordinates x_1^S and x_3^S, and the origin time t_0 assuming that the velocity model is known.

The observed data $\mathbf{d}_{obs}$ and predicted data $\mathbf{d}_{pre}$ are produced by two forward simulations, where $\mathbf{d}_{pre}$ is obtained after perturbing the source parameters used to generate $\mathbf{d}_{obs}$. In both cases, the elastic displacement field $\mathbf{u}(\mathbf{x}^S, \mathbf{x}^{r_n}, t)$ excited by a source located at $\mathbf{x}^S$ is recorded by N receivers located at $\mathbf{x}^{r_n}$ ($n = 1, 2, ..., N$). The data residuals are measured by the least-squares objective function, which has to be minimized by the inversion algorithm:

$$F(\mathbf{m}) = (1/2) \| \mathbf{d}_{pre}(\mathbf{m}) - \mathbf{d}_{obs} \|^2 . \tag{12}$$
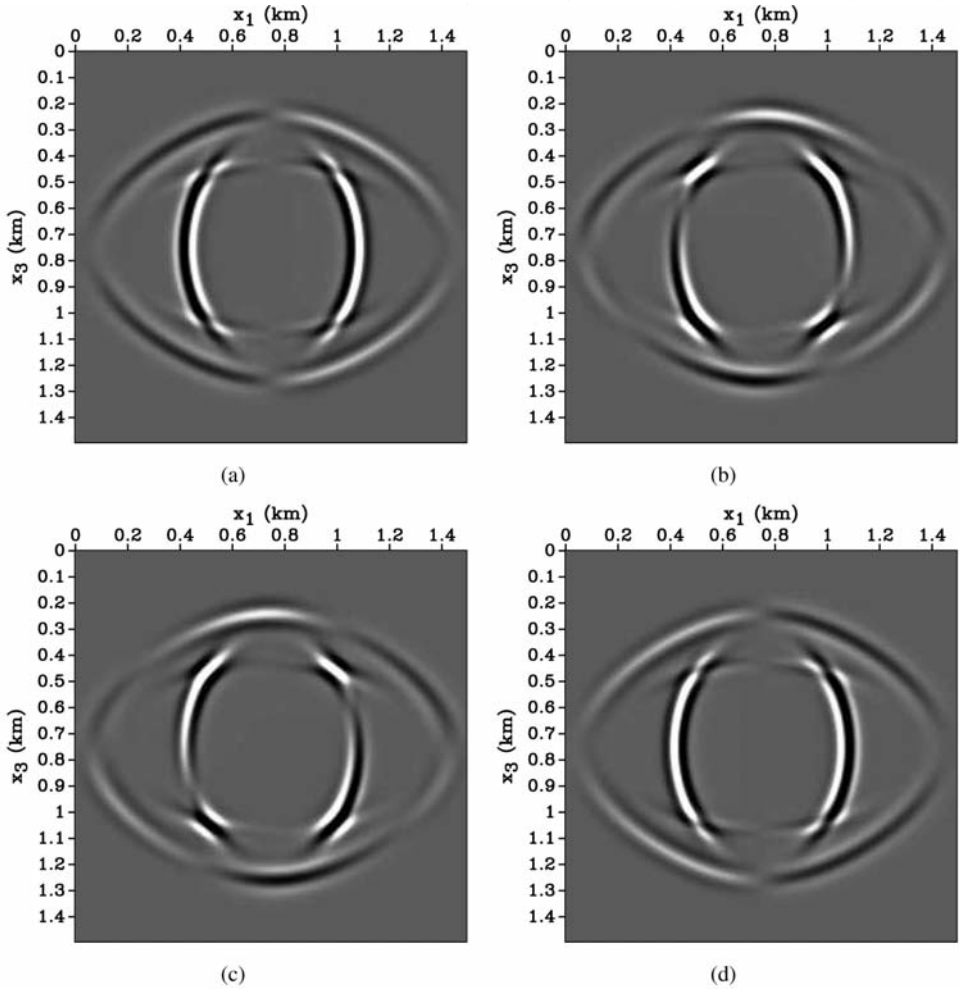
Fig. 2. Vertical displacement generated by dip-slip sources with different orientation (defined by the angle θ) in a homogeneous VTI medium. The medium parameters are $\rho = 2$ g/cm^3, $V_{P0} = 4047$ m/s, $V_{S0} = 2638$ m/s, $\varepsilon = 0.4$, and $\delta = 0$ ($\sigma = 0.94$). The moment tensor is computed from eqs. (9)-(11) with $\Sigma \overline{u} = 1$ m^3 and (a) $\theta = 0°$, (b) $\theta = 30°$, (c) $\theta = 60°$, and (d) $\theta = 90°$.

Application of the adjoint-state method

The objective function depends on the model parameters through the state variables, which represent the solution of the forward-modeling equations. In our case, the state variable is the elastic displacement field $\mathbf{u}(\mathbf{x},t)$ generated by a microseismic source and governed by eq. (3).

Iterative optimization techniques involve calculation of the model update at each iteration. The update direction is determined by the gradient (the derivatives of the objective function with respect to the model parameters), $\partial F(\mathbf{m})/\partial \mathbf{m}$. The adjoint-state method is designed to find this gradient for the entire set of model parameters in just two modeling simulations. However, because this method does not calculate the Fréchet derivatives, it is impossible to evaluate the sensitivity of the solution to perturbation errors.

The adjoint-state method involves the following main steps (Perrone and Sava, 2012):

1. Computation of the state variable (forward wavefield).

2. Computation of the adjoint source.

3. Computation of the adjoint-state variable (adjoint wavefield).

4. Computation of the gradient.

In addition to eq. (3), the method requires solving the adjoint wave equation:

$$\rho(\partial^2 u_i^\dagger/\partial t^2) - c_{ijkl}\,[\partial^2 u_k^\dagger/(\partial x_j \partial x_l)] = \sum_{n=1}^{N} (\mathbf{d}_{\text{obs}} - \mathbf{d}_{\text{pre}})(T - t)\,\delta(\mathbf{x} - \mathbf{x}^{\mathbf{r}_n}) \ , \qquad (13)$$

where $\mathbf{u}^\dagger$ is called the "adjoint wavefield". The so-called adjoint source on the right-hand side of eq. (13) is obtained by differentiating the objective function $F(\mathbf{m})$ with respect to the forward wavefield $\mathbf{u}$, and consists of the time-reversed data residuals. Therefore, the adjoint simulation can be carried out with the same modeling code by "injecting" the adjoint source at the receiver locations and then running the forward simulation.

The derivatives of the objective function with respect to the moment-tensor elements, source coordinates, and origin time can be found as (Kim et al., 2011):

$$\partial F/\partial M_{ij} = \int_0^T \varepsilon_{ij}^\dagger(\mathbf{x}^{\text{ts}}, t)\, S(T - t)\, dt \ , \qquad (14)$$

$$\partial F/\partial x_i^{\text{S}} = \int_0^T \{\partial[\mathbf{M}{:}\varepsilon^\dagger(\mathbf{x}^{\text{ts}}, t)]/\partial x_i\}\,\big|_{\mathbf{x}^{\text{ts}}}\, S(T - t)\, dt \ , \qquad (15)$$

$$\partial F/\partial t_0 = \int_0^T \mathbf{M}{:}\varepsilon^\dagger(\mathbf{x}^{\text{ts}}, t)\,[\partial S(T - t)/\partial t]\, dt \ , \qquad (16)$$

where $\mathbf{x}^{ts}$ is the trial source location, T is the recording time, $\varepsilon^{\dagger} = \frac{1}{2}[\nabla\mathbf{u}^{\dagger} + (\nabla\mathbf{u}^{\dagger})^{T}]$ is defined as the adjoint strain tensor, and $\mathbf{M}:\varepsilon^{\dagger}$ is the double inner product of the tensors $\mathbf{M}$ and $\varepsilon^{\dagger}$. Eqs. (14) - (16) applied to the 2D problem yield the gradient vector $\mathbf{g}$ for the six source parameters:

$$\mathbf{g} = \{(\partial F/\partial M_{11}),(\partial F/\partial M_{13}),(\partial F/\partial M_{33}),(\partial F/\partial x_{1}^{S}),(\partial F/\partial x_{3}^{S}),(\partial F/\partial t_{0})\} \quad . \quad (17)$$

It is interesting that in contrast to the gradient for velocity-related parameters (Liu and Tromp, 2006), which depends on the interaction between the forward and adjoint wavefields, eqs. (14) - (16) include only the adjoint wavefield. This means that there is no need to store or recalculate the forward wavefield during gradient calculation.

When the adjoint-state method is applied to velocity analysis, $\mathbf{u}^{\dagger}$ is supposed to "illuminate" the erroneous parts of the velocity model. Likewise, for the source-inversion problem, $\mathbf{u}^{\dagger}$ reveals the difference in $\mathbf{M}$, $\mathbf{x}^{S}$, and t_{0} that produces the mismatch between the observed and predicted data.

In principle, the number of sources in the adjoint problem is unrestricted. If the forward wavefield is excited by multiple sources, the adjoint wavefield may focus at the actual as well as perturbed (trial) source locations. The areas of focusing make the main contribution to the gradient. However, for inversion purposes we only need the derivatives in eqs. (14) - (16) at the trial source position.

SYNTHETIC TESTS

Next, we present the results of synthetic tests for a homogeneous VTI medium and a stack of three constant-density VTI layers, with the wavefield modeled using the FD code mentioned above.

In the first experiment (Fig. 3), the observed and initial predicted data (Figs. 4 and 5) are generated for a single microseismic event recorded in a vertical "borehole" by receivers located at each grid point. Whereas the observed field is generated by a horizontal dip-slip source ($\theta = 0°$), the predicted field is computed with a vertical source ($\theta = 90°$). Next, the adjoint source "injected" at the receiver locations is used to compute the adjoint wavefield (Fig. 6). This wavefield focuses at the time t = 0.44 s near the actual source, where the model perturbation is located. The focusing time corresponds to the raypath between the source and the receivers located at the end of the array.

After applying eqs. (14) - (16), we obtain the following derivatives for the five source parameters: $\partial F/\partial M_{11} = 0.00038$, $\partial F/\partial M_{13} = 1.28$, $\partial F/\partial M_{33} = $

-0.0022, $\partial F/\partial x_1^S = 2.21$, $\partial F/\partial x_3^S = -0.0039$, and $\partial F/\partial t_0 = -0.82$. The sign of the derivatives (i.e., of the components of the gradient) defines the update direction in the model space, whereas their absolute values determine the magnitude of the update of the corresponding model parameter. The units of the derivatives are not included here because we can compare only the derivatives for the same type of parameters (e.g., for the coordinates x_1^S and x_3^S). The main contribution to the gradient comes from the focusing of the adjoint wavefield near the source location. It may look surprising that the derivatives for x_1^S, x_3^S, and t_0 are nonzero because the values of $\mathbf{x}^S$ and t_0 for the actual and trial sources coincide. However, the derivatives for $\mathbf{x}^S$ and t_0 depend on the components of $\mathbf{M}$, which deviate from the actual values [eqs. (15) and (16)]. Hence, to avoid cycle-skipping problems during the joint inversion for $\mathbf{x}^S$, t_0, and $\mathbf{M}$, a good initial guess is needed for all three types of parameters.

The second test is performed for the three-layer VTI medium in Fig. 7. The actual and trial models have the same source parameters as in the previous experiment. The data are generated by a source placed in the middle layer and recorded by receivers in a vertical "borehole". The derivatives calculated using
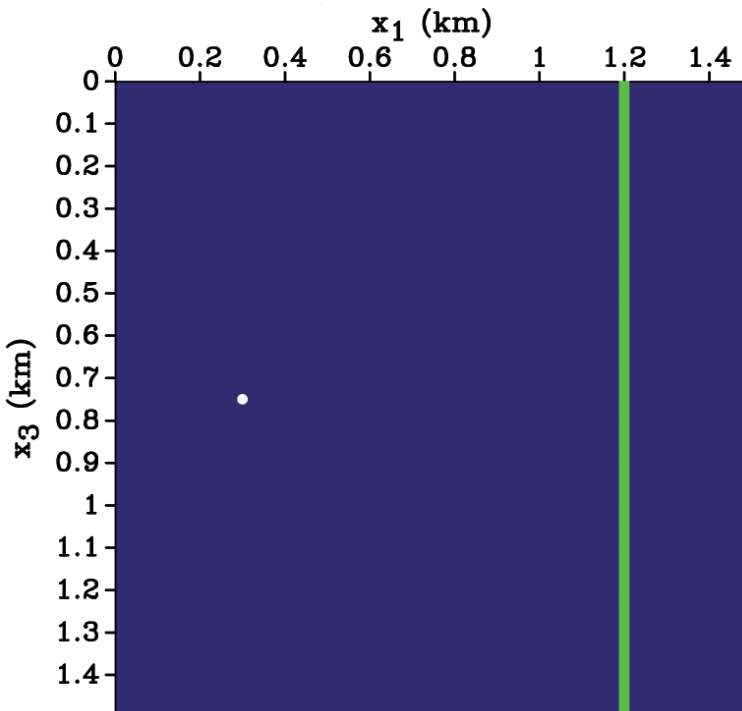

Fig. 3. Source (white dot) and a vertical line of receivers at $x_1 = 1.2$ km embedded in a homogeneous VTI medium. The receivers are placed vertically at each grid point (every 6 m). The medium parameters are $\rho = 2$ g/cm^3, $V_{P0} = 4047$ m/s, $V_{S0} = 2638$ m/s, $\varepsilon = 0.4$, and $\delta = 0$. The source is located at $x_1 = 0.3$ km, $x_3 = 0.75$ km.

the adjoint-state method are $\partial F/\partial M_{11} = 0.004$, $\partial F/\partial M_{13} = 2.44$, $\partial F/\partial M_{33} = -0.0044$, $\partial F/\partial x_1^S = 0.82$, $\partial F/\partial x_3^S = -0.0071$, and $\partial F/\partial t_0 = -0.21$. These derivatives are similar to the ones obtained for the previous test because the tensor M is perturbed in the same way for both cases. The layer boundaries, however, create a number of reflected and mode-converted waves that should make waveform inversion for source parameters better constrained.
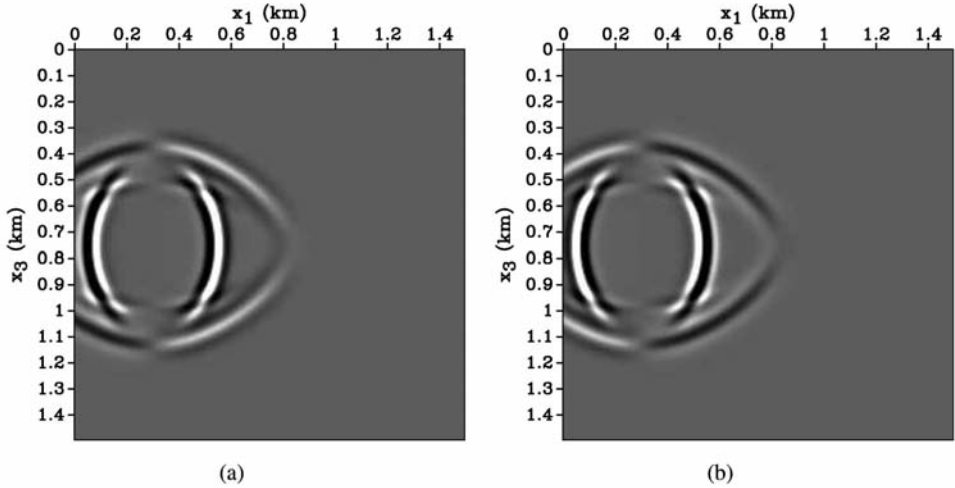
Fig. 4. Snapshots of the vertical displacement for the model in Fig. 3 at $t = 0.14$ s ($\overline{\Sigma u} = 1$ m^3). (a) The observed wavefield produced by a dip-slip source with $\theta = 0°$: (b) The predicted wavefield from a source with $\theta = 90°$.
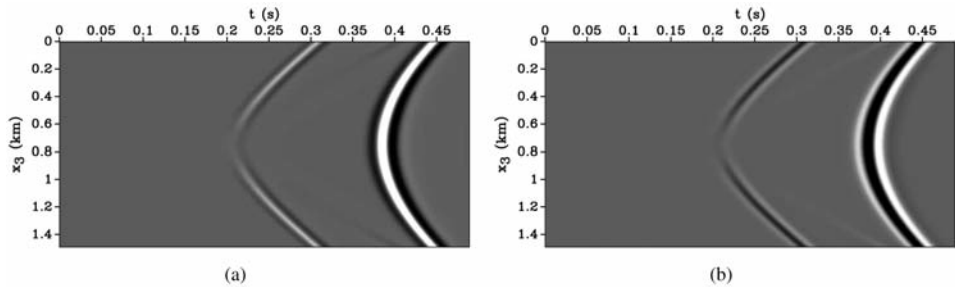
Fig. 5. Vertical displacement of the (a) observed and (b) predicted data for the model in Fig. 3 generated with the source parameters from Fig. 4.
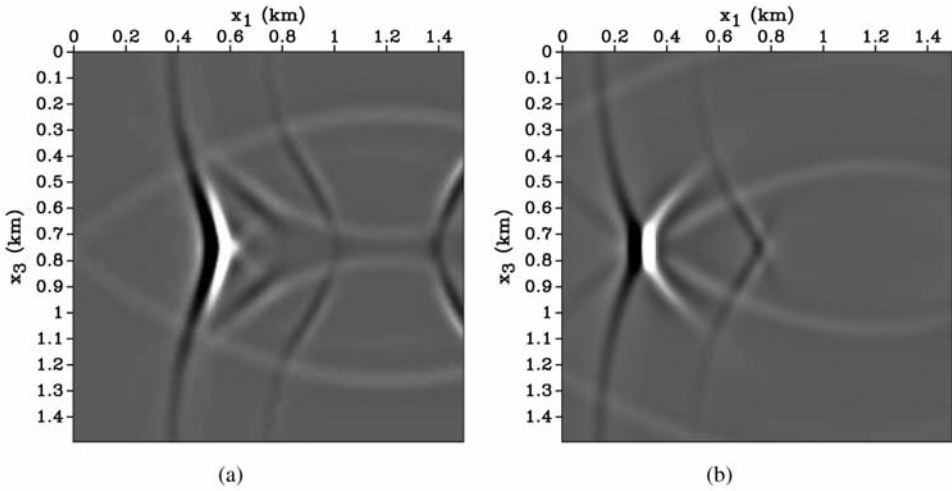
Fig. 6. Snapshots of the vertical component of the adjoint wavefield for the model in Fig. 3 at times (a) $t = 0.35$ s and (b) $t = 0.44$ s. The adjoint wavefield focuses at the actual and trial source locations (which are the same) on plot (b).
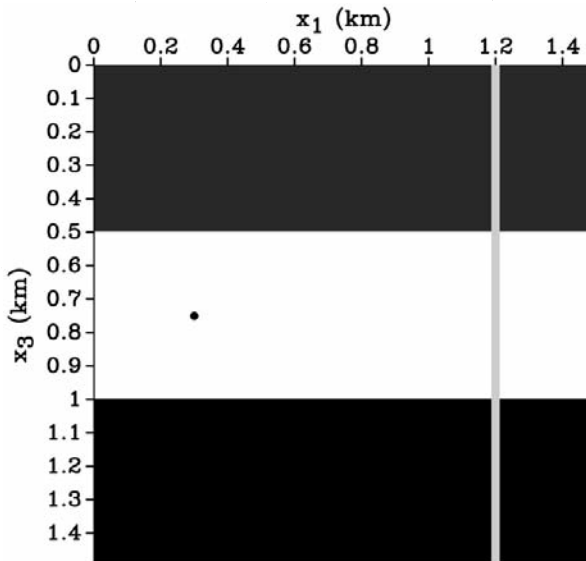

Fig. 7. Three-layer VTI model used in the second experiment. The source-receiver geometry is the same as in Fig. 3. The distance between receivers is 5 m. The parameters $\rho = 2$ g/cm^3, $\varepsilon = 0.4$, and $\delta = 0$ are the same in all three layers. The vertical velocities in the first layer are $V_{P0} = 4047$ m/s and $V_{S0} = 2638$ m/s; for the second layer, $V_{P0} = 4169$ m/s and $V_{S0} = 2320$ m/s; for the third layer, $V_{P0} = 4693$ m/s and $V_{S0} = 2682$ m/s.

For the third experiment, we keep the actual source at the same location as in the previous tests and use the homogeneous model from Fig. 3. This time, the initial trial source is moved horizontally, which generates pronounced gradient contributions at both source locations (Fig. 8). However, as mentioned above, we are interested only in the derivatives computed for the trial source location.
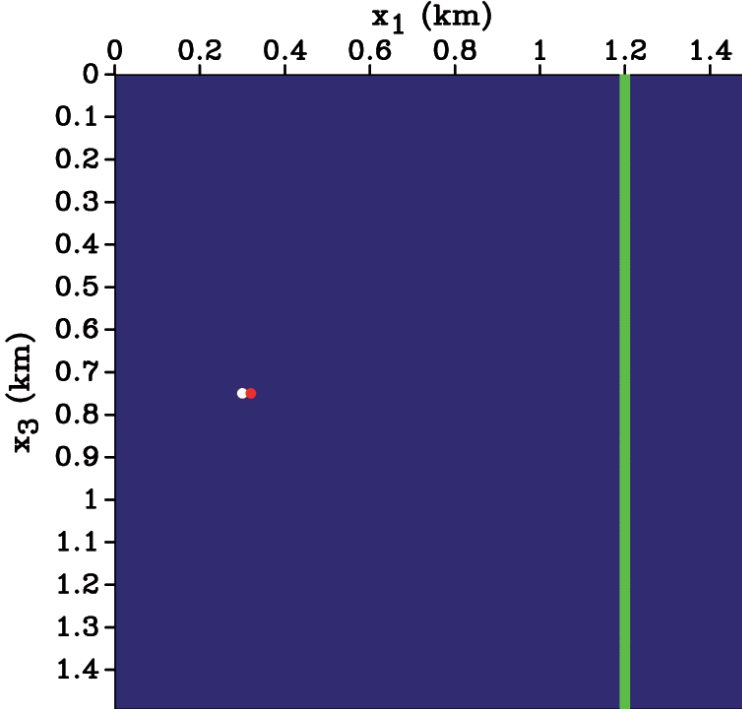

Fig. 8. Actual source (white dot), trial source (red dot) and a vertical line of receivers (spacing is 6 m) embedded in a homogeneous VTI medium. The medium parameters are the same as in Fig. 3. The actual source is located at $x_1 = 0.3$ km, $x_3 = 0.75$ km and the trial source is at $x_1 = 0.32$ km, $x_3 = 0.75$ km. The moment tensor for both sources corresponds to a horizontal ($\theta = 0°$) dip-slip fault with $\Sigma \bar{u} = 1$ m^3.

The obtained derivatives are $\partial F/\partial M_{11} = -0.00017$, $\partial F/\partial M_{13} = -0.25$, $\partial F/\partial M_{33} = 0.00033$, $\partial F/\partial x_1^S = -4.28$, $\partial F/\partial x_3^S = 0.0061$, and $\partial F/\partial t_0 = 1.51$. Although the trial source has the correct moment tensor, the derivatives for M_{11}, M_{13}, and M_{33} do not vanish because the wavefield substantially changes with source location. The derivative for t_0 is also nonzero because moving the source creates traveltime shifts similar to those due to a change in the origin time. Still, the inversion should be able to resolve the trade-off between x^S and t_0 because they influence the traveltimes in a different fashion.

The large value of $\partial F/\partial x_1^S$ compared to $\partial F/\partial x_3^S$ correctly indicates that the trial horizontal source coordinate x_1^S should be updated more significantly than x_3^S. The negative sign of $\partial F/\partial x_1^S$ will lead to a smaller value of x_1^S for the next iteration of inversion, so that the source will move toward its actual position ($x_1 = 0.3$ km).

The last experiment demonstrates a potential application of the adjoint wavefield. The model includes two actual sources with the same tensor **M** and origin time t_0 that generate the wavefield $\mathbf{u}(\mathbf{x},t)$ (Fig. 9). However, we assume that the data $\mathbf{d}_{obs}$ are produced by a single event and specify a single trial source. Then the adjoint wavefield $\mathbf{u}^\dagger$ is expected to focus at two different locations, corresponding approximately to the actual and trial source positions. Instead, the adjoint wavefield actually focuses at three locations (Fig. 10), which helps identify the second source missing in the trial model.

In addition to finding "hidden sources", the field $\mathbf{u}^\dagger$ can be used to improve the initial trial source position because the adjoint wavefield focuses (for the correct velocity model) near the actual source location. This starting source position can be later refined during WI.
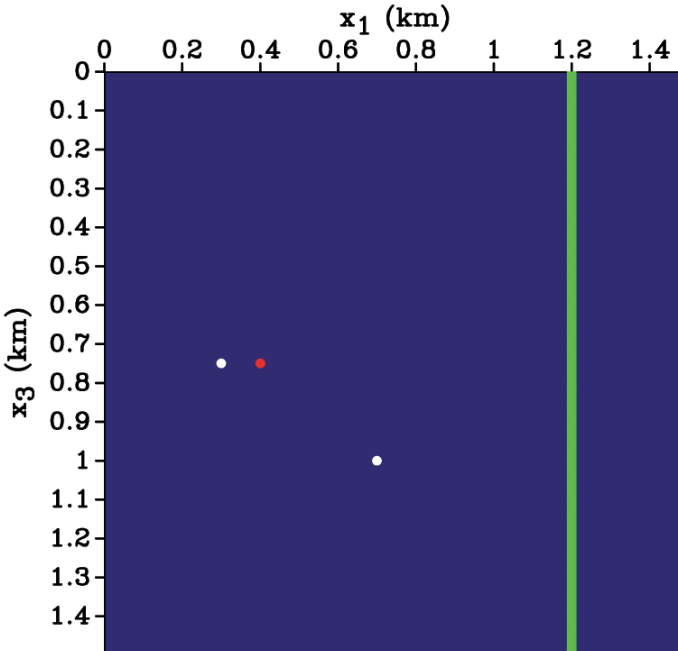

Fig. 9. Two actual sources (white dots), a trial source (red dot), and a vertical line of receivers (the spacing is 6 m) embedded in a homogeneous VTI medium. The medium parameters are the same as in Fig. 3. The actual sources are located at $x_1 = 0.3$ km, $x_3 = 0.75$ km, and $x_1 = 0.7$ km, $x_3 = 1$ km; the trial source is at $x_1 = 0.42$ km, $x_3 = 0.75$ km. The moment tensor for all three sources corresponds to a horizontal ($\theta = 0°$) dip-slip fault with $\Sigma u = 1$ m^3.
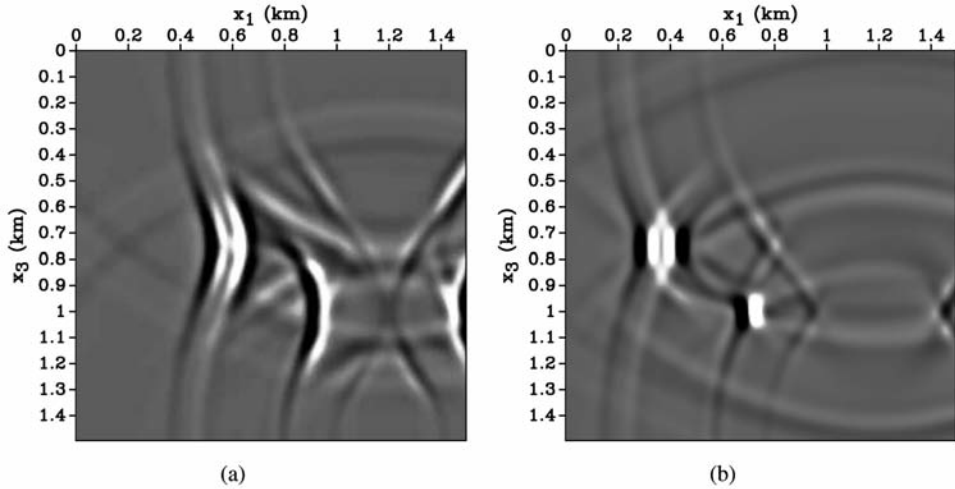
Fig. 10. Snapshots of the vertical component of the adjoint wavefield for the model in Fig. 9 at times (a) $t = 0.32$ s and (b) $t = 0.44$ s. The adjoint wavefield on plot (b) focuses at both actual source locations and at the trial source location.

CONCLUSIONS

Waveform inversion is a potentially powerful tool to solve simultaneously two of the most important problems in microseismic monitoring, event location and source-mechanism estimation. Here, we employed the adjoint-state method to find analytic expressions for the gradient of the WI objective function following the results of Kim et al. (2011). Then adjoint simulations were implemented to calculate the WI gradient for the source location, origin time, and moment tensor using a known VTI velocity model.

Synthetic tests were carried out for multicomponent wavefields from one and two sources recorded by a dense array of receivers in a vertical "borehole". The first experiment was performed for a trial source with a perturbed moment tensor correctly positioned in a homogeneous VTI medium. The adjoint wavefield focuses near the trial source location, which identifies the perturbed area. Although in this experiment the source position was correct, the derivatives for the source coordinates and origin time do not vanish because they depend on errors in the moment-tensor elements.

In the second test, a trial source with a distorted moment tensor was placed in a three-layer VTI model. The additional interfaces produce a more complicated wavefield with a number of reflected and converted waves. These

additional events do not significantly influence gradient calculation but should improve the accuracy and stability of parameter estimation.

The algorithm was also tested for a source with the correct moment tensor and origin time but erroneous location in a homogeneous VTI medium. As in the previous examples, the derivatives of the objective function with respect to the correct parameters (in this case, the moment tensor and origin time) are nonzero. The dependence of the gradient on unperturbed model parameters implies that it is essential to have accurate initial guesses for all unknowns.

Finally, the wavefield was generated by two sources set off simultaneously, while the predicted wavefield was excited by a single source. Focusing of the adjoint wavefield helped us identify the approximate location of the "missing" source. In general, if the velocity model is not strongly distorted, the adjoint wavefield can provide an accurate starting trial source position for waveform inversion.

To take full advantage of the potential of WI in microseismic studies, it can be applied to anisotropic velocity model building as well. This extension will be discussed in a future publication.

REFERENCES

Aki, K. and Richards, P.G., 1980. Quantitative Seismology. Theory and Methods, Vol. I. W.H. Freeman and Co., San Francisco.

Dahlen, F.A. and Tromp, J., 1998. Theoretical Global Seismology. Princeton University Press, Princeton.

Fichtner, A., 2006. The adjoint method in seismology: I. Theory. Phys. Earth Planet. Inter., 157: 86-104.

Fichtner, A., 2009. Full Seismic Waveform Inversion for Structural and Source Parameters. Ph.D. thesis, Ludwig-Maximilians-Universität, Munich.

Gauthier, O., Virieux, J. and Tarantola, A., 1986. Two-dimensional nonlinear inversion of seismic waveforms: Numerical results. Geophysics, 51: 1387-1403.

Grechka, V. and Duchkov, A., 2011. Narrow-angle representations of the phase and group velocities and their applications in anisotropic velocity-model building for microseismic monitoring. Geophysics, 76: WC127-WC142.

Grechka, V., Singh, P. and Das, I., 2011. Estimation of effective anisotropy simultaneously with locations of microseismic events. Geophysics, 76: WC143-WC155.

Grechka, V. and Yaskevich, S., 2013. Azimuthal anisotropy in microseismic monitoring. Part 1: Theory. Expanded Abstr., 83rd Ann. Internat. SEG Mtg., Houston: 1987-1991.

Grechka, V. and Yaskevich, S., 2014. Azimuthal anisotropy in microseismic monitoring: A Bakken case study. Geophysics, 79: KS1-KS12.

Kamath, N. and Tsvankin, I., 2013. Full-waveform inversion of multicomponent data for horizontally layered VTI media. Geophysics, 78: WC113-WC121.

Kendall, M., Maxwell, S., Foulger, G., Eisner, L. and Lawrence, Z., 2011. Microseismicity: Beyond dots in a box. Introduction. Geophysics, 76: WC1-WC3.

Kim, Y., Liu, Q. and Tromp, J., 2011. Adjoint centroid-moment tensor inversions. Geophys. J. Internat., 186: 264-278.

Köhn, D., 2011. Time Domain 2D Elastic Full Waveform Tomography. Ph.D. thesis, Christian Albrechts-Universiät, Kiel.

Lee, H.-Y., Koo, J.M., Min, D.-J., Kwon, B.-D. and Yoo, H.S., 2010. Frequency-domain elastic full waveform inversion for VTI media. Geophys. J. Internat., 183: 884-904.

Li, J., Toksöz, M.N., Li, C., Morton, S., Dohmen, T. and Katahara, K., 2013. Locating Bakken microseismic events with simultaneous anisotropic tomography and extended double-difference method. Expanded Abstr., 83rd Ann. Internat. SEG Mtg., Houston: 2073-2078.

Liu, Q. and Tromp, J., 2006. Finite-frequency kernels based on adjoint methods. Bull. Seismol. Soc. Am., 96: 2383-2397.

Maxwell, S., 2010. Microseismic: Growth born from success. The Leading Edge, 29: 338-343.

Mora, P., 1987. Nonlinear two-dimensional elastic inversion of multioffset seismic data. Geophysics, 52: 1211-1228.

Morency, C. and Mellors, R.J., 2012. Full moment tensor and source location inversion based on full waveform adjoint inversion: application at the Geysers geothermal field. Expanded Abstr., 82nd Ann. Internat. SEG Mtg., Las Vegas: 1-5.

Perrone, F. and Sava, P., 2012. Wavefield tomography based on local image correlations: CWP Project Review Report: 51-76.

Plessix, R.-E., 2006. A review of the adjoint-state method for computing the gradient of a functional with geophysical applications. Geophys. J. Internat., 167: 495-503.

Pratt, R.G., 1999. Seismic waveform inversion in the frequency domain, Part 1: Theory and verification in a physical scale model. Geophysics, 64: 888-901.

Tarantola, A., 1984. Inversion of seismic reflection data in the acoustic approximation. Geophysics, 49: 1259-1266.

Thomsen, L., 1986. Weak elastic anisotropy. Geophysics, 51: 1954-1966.

Tromp, J., Tape, C. and Liu, Q., 2005. Seismic tomography, adjoint methods, time reversal and banana-doughnut kernels. Geophys. J. Internat., 160: 195-216.

Tsvankin, I., 2012. Seismic Signatures and Analysis of Reflection Data in Anisotropic Media, 3rd ed. SEG, Tulsa, OK.

Tsvankin, I. and Grechka, V., 2011. Seismology of Azimuthally Anisotropic Media and Seismic Fracture Characterization. SEG, Tulsa, OK.

Van Dok, R., Fuller, B., Engelbrecht, L. and Sterling, M., 2011. Seismic anisotropy in microseismic event location analysis. The Leading Edge, 30: 766-770.

Vavryčuk, V., 2005. Focal mechanisms in anisotropic media. Geophys. J. Internat., 161: 334-346.

Vavryčuk, V., 2007. On the retrieval of moment tensors from borehole data. Geophys. Prosp., 55: 381-391.

Virieux, J., and Operto, S., 2009. An overview of full-waveform inversion in exploration geophysics. Geophysics, 74: WCC1-WCC26.